Compressive Sensing Techniques for Radar and ESM Applications:

Part I: Application of Compressive Sensing to 2D/3D SAR

Emre Ertin

Department of Electrical and Computer Engineering

The Ohio State University

Columbus, Ohio

1.0 Application of Compressive Sensing to 2D/3D SAR

1.1 Introduction

In this chapter, we consider the problem of 2D and 3D imaging of targets from radar data obtained from wide-angle sparse synthetic apertures. These reconstructions are enabled by new data collection capabilities, in which airborne synthetic aperture radar (SAR) systems are able to interrogate a scene, such as a city, persistently and over a large range of aspect angles. Additional information provided by wide-aspect 3-D reconstructions can be useful in applications such as automatic target recognition (ATR) and fingerprinting.

We consider an airborne radar sensor which transmits sideband pulsed waveforms along a flight path and records the backscatter response from the scene. The returned echoes can be interpreted as 1-D line segments of the 3-D Fourier transform of the scene, and the aggregation of radar returns over the flight path defines a conical manifold of data in the scenes 3-D Fourier domain. These samples in the Fourier Domain can be projected to a 2D plane to obtain SAR Imagery. However, generating high-resolution 3-D images using traditional Fourier processing methods requires that radar data be collected over a densely sampled set of points in both azimuth and elevation angle. This method of imaging requires very large collection times and data storage and may be prohibitively costly in practice, since the aircraft has to make a large number of passes to sample along the elevation dimension. There is thus motivation to consider more sparsely sampled data collection strategies, where only a small fraction of the data required to perform traditional high-resolution imaging is collected. However, when Fourier imaging is applied to sparsely sampled apertures, reconstruction quality suffers in either resolution or high sidelobes or both.

In this chapter, we survey several of the techniques [1–11] that have been recently proposed for 3-D reconstruction data collected from sparsely apertures where the radar sensor collects information from few passes

at slightly different elevation angles. These techniques rely on some basic properties of scattering physics, and exploit signal sparsity (in the reconstruction domain) of radar scenes. Man-made target scenes are dominated by a sparse number of dominant isolated scattering centers; dominant returns result from objects such as corner or plate reflectors made from electromagnetic conductive material of different dielectric properties. Therefore the inversion problem can be regularized using sparsity constraints in the image domain. We will review both 3-D versions of L_p norm regularized least-square approaches popularized by compressive sensing field as well as wide-angle extension of multibaseline interferometric synthetic aperture radar (IFSAR) approaches that rely on spectral-estimation methods in the height dimension.

Wide-angle imaging problems differ from traditional techniques designed for *narrow* angle collection geometries, where isotropic scattering assumption is well-approximated. For wide-angle scenes, radar scattering is typically anisotropic over wide angles and violates the isotropic point scattering assumption of traditional radar imaging. Anisotropic scattering over wide angles is addressed in each case by using non-coherent subaperture imaging, where scattering is assumed to be isotropic over narrow-angle subapertures.

In the following, we first review the system model for wide-angle SAR collections and discuss shortcomings of the traditional Fourier imaging methods when applied to sparse circular synthetic aperture (CSAR) collections. Throughout the chapter, we use AFRL GOTCHA CSAR data set [12] for comparative empirical results. GOTCHA CSAR data set is fully polarimetric and consists of eight complete circular passes, with each pass being at a slightly different elevation angle. The radar used in the GOTCHA data collection has a center frequency of 9.6 GHz and a bandwidth of 640 MHz. Next, we present a direct 3-D imaging approach based on sparsity regularized inversion of the CSAR measurement operator with empirical results and discuss computational complexity of the direct approach. Then, we review multi baseline IFSAR techniques for this problem and consider interpolated array methods and discrete Fourier transform (DFT) peak detection methods, and present empirical results in each case. We conclude with a discussion of practical

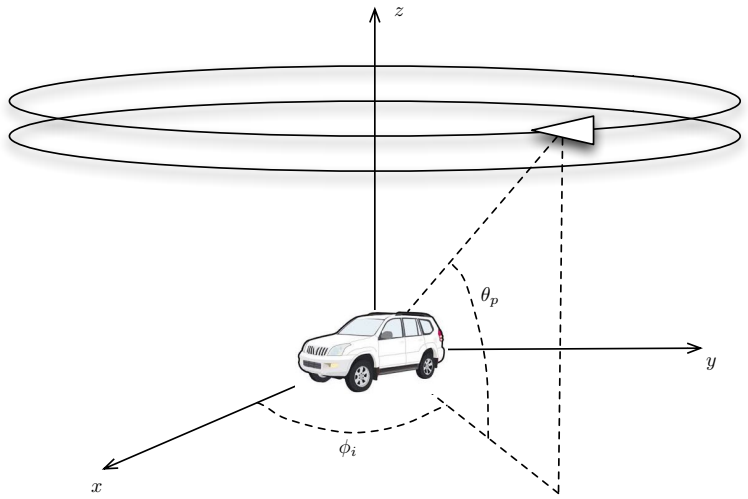

Figure 1: Multipass Circular SAR Data Collection Geometry.

considerations such as data registration and autofocus for obtaining accurate reconstructions.

1.2 System Model

In this section, we present the system model for circular synthetic aperture radar (CSAR) data collections and briefly review traditional Fourier imaging with CSAR data. We assume that the SAR system collects coherent backscatter measurements $g_{i,p}(f_k)$ on circular apertures parameterized with azimuth angles $\{\phi_i\}$ covering $[0, 2\pi]$ and at a set of elevation angles $\{\theta_p\}_{p=1}^{P}$ collected over different passes of the aircraft. Figure 1 shows the multipass CSAR collection geometry. The radar transmits a wideband signal with bandwidth B centered about a center frequency f_c. Such a signal could be an FM chirp signal or a stepped-frequency signal, but other wideband signals can also be used. We also assume that the transmitter is sufficiently far away from the scene so that wavefront curvature is negligible, and we use a plane wave model for reconstruction; this assumption is valid, for example, when the extent of the scene being imaged is much smaller than the standoff distance from the scene to the radar.

The backscatter measurements are taken at discrete set of frequencies given by the set $\{f_k\}$. The imaging

problem is to estimate the three-dimensional reflectivity function of the spotlighted scene $f(x, y, z)$ from the set of radar returns $\{g_{i,p}(f_k)\}$ collected by the radar. The three-dimensional version of the projection-slice theorem shows that the backscatter measurements represent samples of the 3-D spatial Fourier transform of the reflectivity function [13]. Specifically, the 3-D Fourier transform $G(k_x, k_y, k_z)$ of the reflectivity function $g(x, y, z)$ is given by:

$$G(k_x, k_y, k_z) = \int g(x, y, z) e^{-j(k_x x + k_y y + k_z z)} \, \mathrm{d}\mathbf{r}. \tag{1}$$

where $\mathbf{r} = (x, y, z)$ is a vector of spatial coordinates. Then, the radar measurements $\{g_{i,j}(f_k)\}$ correspond to the samples of $G(k_x, k_y, k_z)$ on a two-dimensional conical manifold at points $(k_x^{i,p,k}, k_y^{i,p,k}, k_z^{i,p,k})$:

$$\begin{aligned} k_x^{i,p,k} &= \frac{4\pi f_k}{c} \cos(\theta_p) \cos(\phi_i) \\ k_y^{i,p,k} &= \frac{4\pi f_k}{c} \cos(\theta_p) \sin(\phi_i) \\ k_z^{i,p,k} &= \frac{4\pi f_k}{c} \sin(\theta_p) \end{aligned}$$

The inverse Fourier Transform of the data calculated on each conical manifold indexed by the elevation cut p results in a wide-angle volumetric image $I_p(x, y, z)$. The sum of all the volumetric images $I_p(x, y, z)$ results in the final coherent wide-angle volumetric image $I(x, y, z)$:

$$I(x, y, z) = \sum_p I_p(x, y, z) \tag{2}$$

We note that any 2-D slice from $I_p(x, y, z)$ contains all the information from the single pass, and in particular all 2-D slices can be regenerated from the ground plane image $I_p(x, y, 0)$ using:

$$I_p(x, y, z) = \mathcal{F}^{-1}_{(x,y)} \left[\mathcal{F}_{(x,y)}[I_j(x, y, 0)] e^{-j\sqrt{k_x^2 + k_y^2} \tan(\theta_j) z} \right] \tag{3}$$

Consequently, a 2-D ground plane image $I_p(x, y, 0)$ from each elevation θ_p is sufficient to construct the coherent volumetric image $I(x, y, z)$. However, the set of wide-angle images $I_p(x, y, 0)$ is not an efficient data representation for the radar returns, because it requires a high spatial sampling rate to prevent aliasing

of the circular bandpass signature given by: z

$$\delta_x < \frac{c}{4\cos(\theta)(f_c + \mathrm{B}/2)} \tag{4}$$

resulting in a Nyquist sampling rate of 1 centimeter for an X-band radar. In addition, 360 degree imagery is matched to an isotropic point scatterer that persists over the entire circular aperture. To minimize the storage of CSAR data, while providing image products matched to scatterers with limited persistance, we adopt image sequences $\{I_{p,m}(x,y,0)\}_m$ where each image is the output of a filter matched to a limited-persistence reflector over the azimuth angles in window $\mathcal{W}_m(\phi)$. Specifically, the m-th subaperture image is constructed using

$$I_{p,m}(x,y,0) = \tag{5}$$
$$\mathcal{F}^{-1}_{(x,y)}\left[F(k_x,k_y,\sqrt{k_x^2+k_y^2}\tan(\theta_j))\mathcal{W}_m(\tan^{-1}\frac{k_x}{k_y})\right]$$

where the azimuthal window function $\mathcal{W}_m(\phi)$ is defined as:

$$\mathcal{W}_m(\phi) = \begin{cases} W\left(\frac{\phi-\phi_m}{\Delta}\right), & -\Delta/2 < \phi < \Delta/2 \\ 0, & \text{otherwise} \end{cases} \tag{6}$$

Here, ϕ_m is the center azimuth angle for the m-th window and Δ describes the hypothesized persistence width. The window function $W(\cdot)$ is an invertible tapered window used for cross-range sidelobe reduction. We also note that unlike the full 360 degree image, each image can be modulated to baseband and sampled at a lower resolution without causing aliasing. Each baseband image $I^B_{p,m}(x,y,z)$ is calculated as:

$$I^B_{p,m}(x,y,0) = I_{p,m}(x,y,0)e^{-j(k_x^0(m)x+k_y^0(m)y)}. \tag{7}$$

where the center frequency $(k_x^0(m), k_y^0(m))$ is determined by the center aperture ϕ_m, mean elevation angle $\bar{\theta}$ and center frequency f_c.

$$\begin{aligned} k_x^0 &= \frac{4\pi f_c}{c}\cos(\bar{\theta})\cos(\phi_m), \\ k_y^0 &= \frac{4\pi f_c}{c}\cos(\bar{\theta})\sin(\phi_m). \end{aligned}$$

For small azimuth windows Δ, the Nyquist sampling rate for each image $I^B_{p,m}(x, y, 0)$ is dictated by the radar bandwidth and results in much smaller storage requirement for CSAR data. We note that the reduction in sampling requirement is a result of subaperture imaging and not baseband processing. Subaperture imaging limits the 2-D spectral extent to a patch whose size is proportional to the radar bandwidth. In contrast, full 360° degree CSAR image occupies an annulus at Fourier domain with radius dictated by the center frequency, necessitating much higher sampling frequency.

We note that the center frequency $(k^0_x(m), k^0_y(m))$ used in baseband modulation is independent of the elevation angle θ_p. The use of common center frequency preserves the relative phase information between the elevation cuts. The relative phase information between the images $I_{p,m}(x, y, 0)$ corresponding passes is key to resolving the height dimension and producing three dimensional imagery as described in sections 1.4 and 1.5.

The image sequence $\{I^B_{p,m}(x, y, 0)\}_m$ can be enhanced by deconvolving the subaperture point spread function [14] and can be visualized in many different ways. One possibility is to use generalized likelihood ratio test (GLRT) imaging proposed by Moses and Potter [15]. The GLRT image $I_G(x, y, z)$ can be obtained by taking a maximum over the sub-aperture imagery:

$$I_G(x, y, z) = \max_m |\sum_p I^B_{p,m}(x, y, z)| \tag{8}$$

1.3 Case Study for 3-D SAR: AFRL GOTCHA Volumetric SAR Data Set

To provide empirical results for the 3-D imaging techniques presented in this chapter, we use AFRL GOTCHA CSAR data set [12], which is fully polarimetric and consists of eight complete circular (360°) passes, with each pass being at a different elevation angle, θ_p; the radar used in the GOTCHA data collection has a center frequency of 9.6 GHz, giving a center wavelength of $\lambda_c = 0.031$, and a bandwidth of 640 MHz. Figure 2 shows the eight passes in a global coordinate system, where the z dimension is height as measured from the

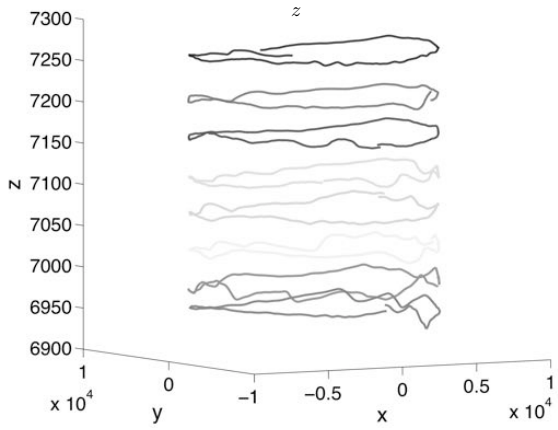

Figure 2: Eight passes from GOTCHA CSAR collection. (Unit dimension is meter).

ground plane in meters. This figure demonstrates the change in elevation angle across each pass.

Defining the height dimension with respect the slant plane coordinate system as z_{S}, and height in a global ground plane coordinate system as z_{G}, if data is uniformly sampled in z_{S}, resolution ρ in the height dimension of the respective coordinate systems is given by

$$\rho_{\mathrm{S}} = \frac{\lambda_c}{2\theta_{\mathrm{ext}}} \text{ m} \qquad \rho_{\mathrm{G}} = \frac{\lambda_c \cos(\theta)}{2\theta_{\mathrm{ext}}} \text{ m}, \tag{9}$$

and spatial aliasing in the height dimension occurs at

$$\mathrm{Alias}_{\mathrm{S}} = \frac{\lambda_c}{2\Delta\theta} \text{ m} \qquad \mathrm{Alias}_{\mathrm{G}} = \frac{\lambda_c \cos(\theta)}{2\Delta\theta} \text{ m}, \tag{10}$$

where θ_{ext} is the extent of the aperture in elevation angle. For the GOTCHA dataset, images formed using all 8 ideal passes, $\Delta\theta = 0.18°$, $\theta_{\mathrm{ext}} = 1.29°$, a slant plane elevation of $\theta = 45°$, have resolution in the height dimension of $\rho_{\mathrm{S}} = 0.69$ m, and $\rho_{\mathrm{G}} = 0.49$ m, and aliasing in the height dimension of $\mathrm{Alias}_{\mathrm{S}} = 4.97$ m, and $\mathrm{Alias}_{\mathrm{G}} = 3.51$ m. We note that since the actual flight paths vary in elevation and are not uniformly sampled in height, the point spread function of the SAR imager will not, in general, have a sinc-like structure. As a result, sidelobes of the point spread function (PSF) function have non-negligible magnitude limiting the resolution beyond the limits derived by the uniform sampling assumption. Figure 3 shows a traditional volumetric SAR image of a Ford Taurus station wagon. The side of the car is parallel to the y axis, with

the front of the car being at the most negative y value. The images show a profile of the car with the front portion of the car sloping up to the rear domed shape section of the car. Non-linear flight path imaging artifacts result in a point spread function with strong sidelobes in slant-plane height direction. This manifests itself as artifacts both above and below the car, degrading image quality.

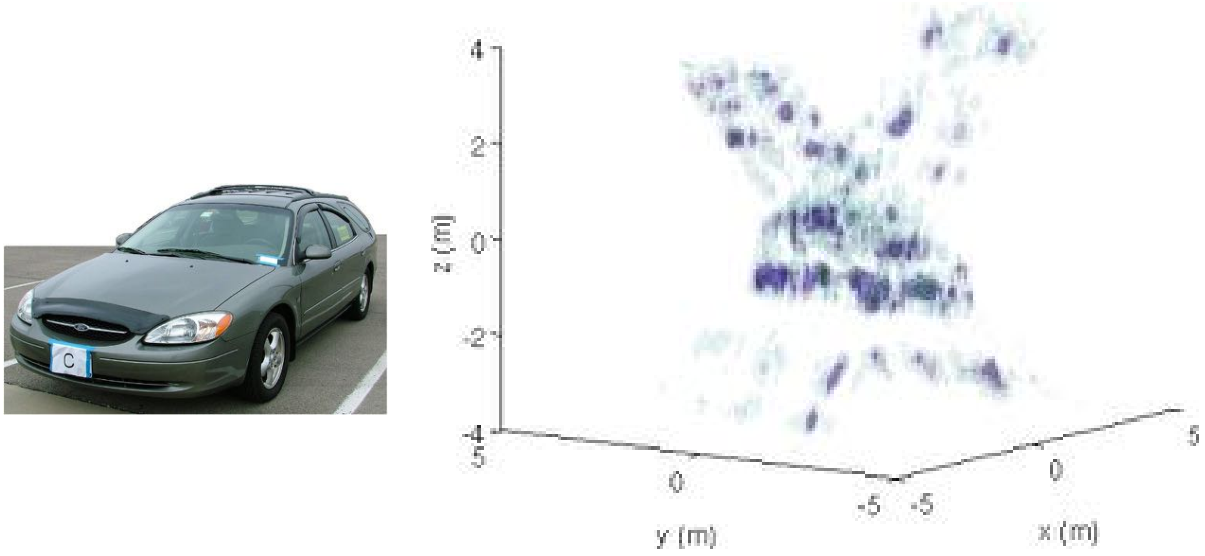

(a) Photo of Taurus station wagon

(b) 3-D GLRT SAR image

Figure 3: Photo of a Taurus station wagon and 3-D backprojection image formed using 8 passes of GOTCHA data.

1.4 Direct Approach to Sparsity Regularized 3-D Construction

The direct approach to 3-D imaging presented in this section is applicable to arbitrary data collection scenarios including the sparse collections that is of interest to urban scenarios. This approach [1, 5] assumes that the number of 3-D locations in which nonzero backscattering occurs is sparse in the 3-D reconstruction space, and applies sparse reconstruction techniques to regularize the resulting inverse problem. The reconstruction problem is posed as an L_p regularized least-squares (LS) problem, where the regularizing term encourages sparse solutions. This L_p regularized least-square imaging algorithm tries to maximize to fit an image domain scattering model to the measured k-space data, using a regularization term that penalizes

the number of non-zero voxels. The algorithm makes the assumption that the complex magnitude response of each scattering center is approximately constant over the aspect angles and across the radar frequency bandwidth. In contrast to the algorithms presented in sections 1.5.1 and 1.5.2, which apply to collections consisting of approximately parallel apertures, the direct approach presented in this section does not make any *a priori* assumptions on the collection geometry. Let $C = \{(x_n, y_n, z_n)\}_{n=1}^{N}$ be the set of volumetric N grid points in image reconstruction space. Typically these locations are chosen on a uniform grid to facilitate fast computations. The $M \times N$ data measurement matrix is given by

$$\mathbf{\Phi} = \left[e^{-j(k_{x,m}x_n + k_{y,m}y_n + k_{z,m}z_n)} \right], \tag{11}$$

where m indexes M measured k-space frequencies down rows, and n indexes the N coordinates in the volumetric grid C across columns. Under the assumption that scattering center amplitude is constant over the aspect angle extent and radar bandwidth considered, the measured (subaperture) data from the scattering center model, can be written in matrix form as

$$\boldsymbol{y} = \mathbf{\Phi}\boldsymbol{x} + \boldsymbol{n}, \tag{12}$$

where $\boldsymbol{x}$ is the N-dimensional vectorized 3-D image representing the scene in the view of the radar, The scene $\boldsymbol{x}$ is assumed to have nonzero complex reflectivity in the j'th row if a scattering center is present at the location (x_j, y_j, z_j) and is zero in row j otherwise; the spatial vector $\boldsymbol{x}$ maps to the 3-D image, $I(x_j, y_j, z_j)$, through $I(x_j, y_j, z_j) = \boldsymbol{x}_j$. Column i of $\mathbf{\Phi}$ corresponds to the response of a unit amplitude scatterer placed at location (x_i, y_i, z_i). The noise vector $\boldsymbol{n}$ is an M dimensional i.i.d. circular complex Gaussian noise vector with zero mean and variance σ_n^2, and the measurement vector $\boldsymbol{y}$ is an M-dimensional vector of noisy k-space measurements. The reconstructed image, $\boldsymbol{x}$, is the solution to the sparse optimization problem [16,17]

$$\boldsymbol{x}^* = \arg\min_{\boldsymbol{x}} \left\{ \|\boldsymbol{y} - \mathbf{\Phi}\boldsymbol{x}\|_2^2 + \lambda \|\boldsymbol{x}\|_p^p \right\}, \tag{13}$$

where the p-norm is denoted as L_p , $0 < p \leq 1$, and λ is a sparsity penalty weighting parameter. Many algorithms exist for solving (13) or the constrained version of this problem when $p = 1$ (e.g. [18–21]), or in

the more general case, when $0 < p \leq 1$ (e.g. [17, 22]). We note that the model in (1) assumes the scatterers are anisotropic for each polarization, the image must be formed for each narrow-angle subaperture and polarization, and then combine non-coherently using (8). Alternatively approaches for joint reconstruction of multiple images proposed in [6] may also be applied to simultaneously reconstruct all polarizations for each subaperture.

Figure 4: L_p regularized least-square reconstructions of a civilian vehicle from GOTCHA dataset (3-D, Side and Top Views, p = 1 and λ = 10).

We form 3-D reconstructions of two spotlighted areas of the CSAR GOTCHA scene centered on a Toyota Camry parked stationary. For the L_p regularized LS reconstructions, 5° subapertures with no overlap were used, for a total of 72 subaperture images that are combined by (8). Reconstructed L_p regularized LS image voxels are spaced at 0.1 m in all three dimensions. The dimensions of the reconstructed tophat and Camry images in (x, y, z) dimensions are $[-2, 2) \times [-2, 2) \times [-2, 2)$ and $[5, 5) \times [-5, 5) \times [-5, 5)$ meters respectively. For the results shown in Figure 4, we chose $p = 1$ and $\lambda = 10$ experimentally to generate images that produce qualitatively good reconstructions. For each figure only voxels whose energy is within the top 40dB of image maximum is shown. To highlight vehicle structure, images are displayed using a smoothing interpolation with Gaussian kernel standard deviation of $\sigma = 0.1$m. The apparent artifacts below the front of the car and to the side of the car in the 3-D view, are scattering from an adjacent vehicle that is not completely removed by the spotlighting process.

1.4.1 Algorithmic and Computational Considerations

In general, sparsity regularized direct inversion of the 3-D problem require considerable memory and computational resources. For our simulation results we use the iterative majorization-maximization algorithm due to [17] to solve (13), which is applicable to the case $0 < p \leq 1$. In each iteration of the algorithm a majorizing function $J(x, x^{(k)})$ that lower-bounds the original cost function is optimized, and the sequence of optimum solutions converges to the solution of the original optimization problem. The majorizing cost function $J(x, x^{(k)})$ is defined as:

$$J(x, x^{(k)}) = \|\boldsymbol{y} - \boldsymbol{\Phi}\boldsymbol{x}\|_2^2 + \lambda \sum_{i=1}^{N} h(\boldsymbol{x}_i, \boldsymbol{x}_i^{(k)}), \tag{14}$$

where superscript (k) is the iteration number; subscript i is the component index of the vector $\boldsymbol{x}$, and

$$h(\boldsymbol{x}_i, \boldsymbol{x}_i^{(k)}) = |\boldsymbol{x}_i^{(k)}|^p + \text{Re}\left\{p(\boldsymbol{x}_i^{(k)})^* |\boldsymbol{x}_i^{(k)}|^{p-2}(\boldsymbol{x}_i - \boldsymbol{x}_k^i)\right\} + \frac{1}{2}p|\boldsymbol{x}_i^{(k)}|^{p-2}|\boldsymbol{x}_i - \boldsymbol{x}_i^{(k)}|^2. \tag{15}$$

It was shown in [17] that the sequence of solutions

$$\boldsymbol{x}^{k+1} = \arg\min J(\boldsymbol{x}, \boldsymbol{x}^{(k)}) \tag{16}$$

$$= \left[\boldsymbol{\Phi}^H\boldsymbol{\Phi} + \frac{\lambda}{2}D(\boldsymbol{x}^{(k)})\right]^{-1}\boldsymbol{\Phi}^H\boldsymbol{y}, \tag{17}$$

where $D(\boldsymbol{x}^{(k)}) = \text{diag}\{p|\boldsymbol{x}_i^{(k)}|^{p-2}\}$, converges to the solution to of the L_p regularized LS problem. For the image reconstruction problems considered here, conjugate gradient (CG) algorithm [16] provides a computationally efficient method to perform the matrix inversion in (17). This results in an algorithm with two nested loops: The outer loop iterates on the solution $\boldsymbol{x}^{(k)}$, and the inner loop is the CG loop that computes the matrix inversion. Proper termination criteria for both loops have to be implemented to achieve to a proper solution. Typically, the outer loop is terminated when the relative change in the original objective function is small between iterations, and we the inner CG loop is terminated, when the relative magnitude of the residual becomes small.

In practice, the inner loop terminates after very few iterations for a Fourier operator, as the case in here. In our experience, this type of algorithm terminates faster than a split Bregman iteration approach [21] for the imaging problems considered here. Let $\Delta_x, \Delta_y, \Delta_z$ be the voxel spacings in the uniform rectilinear grid C. Then, the coordinates in the C consist of all permutations of (x, y, z) coordinates from the partitioned axes; and the set C defines a uniform 3-D grid on the scene. If, in addition, we assume that the k-space samples lie on a uniform 3-D frequency grid centered at the origin, the operation $\boldsymbol{\Phi x}$ can be implemented using the computationally efficient 3-D Fast Fourier Transform (FFT) operation. In many scenarios, including the one here, the measured k-space samples are not on a uniform grid, and therefore the FFT cannot be used directly. A potential solution would be to first interpolate the k-space samples and then apply the standard FFT operation to the interpolated samples. A computationally efficient, alternative approach is to use Type-2 nonuniform FFTs (NUFFT)s as the operator $\boldsymbol{\Phi}$ to process data directly on the non-uniform k-space grid, as given in [23, 24]. The implementation of nonuniform FFT algorithms require an interpolation step executed for each evaluation of $\boldsymbol{\Phi}$; whereas, in interpolate then FFT approach, the interpolation occurs only once. As a result for an iterative algorithm where repeated evaluation of the $\boldsymbol{\Phi}$ is required, the latter approach might be preferred. For apertures proportional to the bandwidth resulting in square-pixels, simple nearest neighbor interpolation provides is sufficient.

For an iterative algorithm, like the one utilized here, only the data vector $\boldsymbol{y}$ as well as the current iterate of $\boldsymbol{x}$ and a gradient with the same dimension as $\boldsymbol{x}$ needs to be stored. For example, to reconstruct a scene of size of a single vehicle, $N = 256^3 \approx 1.7 \cdot 10^7$ are required. Therefore, for reconstructing of a vehicle, a minimum of three vectors of size $1.7 \cdot 10^7$ should be stored at double precision with complex valued variables. For algorithms that utilize a conjugate gradient approach for matrix inversion it is necessary to store a conjugate vector of dimension N as well. Whereas in a Newton-Raphson approach, it is necessary to store a Hessian of dimension $N \times N$. During each iteration of the recovery algorithm, the operator $\boldsymbol{\Phi}$ and its adjoint has to be computed. These operations can become very computationally expensive when the

problem size grows and may result in a computationally intractable algorithm, unless a fast operator such as the FFT is employed. Specifically, since $\mathbf{\Phi}$ is an $M \times N$ matrix, direct multiplication of $\mathbf{\Phi}\boldsymbol{x}$ requires MN multiplies and additions per evaluation. For the examples considered in this section, the average value of these M values is 105, requiring $MN \approx 10^{12}$ operations. In contrast after an initial interpolation step, an FFT implementation of $\mathbf{\Phi}\boldsymbol{x}$ requires $\mathcal{O}(D^3 \log(D^3))$ operations, where D is the maximum number of samples across the image dimensions. For the imaging example, with $D = 256$, FFT implementation results in computational savings on the order of 10^3.

1.5 Multiple Elevation IFSAR

In this section, we consider a parametric method for high resolution 3-D reconstruction for multipass circular SAR. Multibaseline generalizations of IFSAR have been considered for linear collection geometries in [25, 26], here we consider parametric spectral estimation techniques for 3-D target reconstruction in circular SAR systems.

The input to the multipass IFSAR algorithm is a set of baseband modulated ground plane images $\{I^B_{p,m}(x, y, 0)\}_p$ at a given subaperture centered ϕ_m of data collected at elevation pass θ_p. For notational simplicity we drop common indices and denote the image sequence as $\{I_p(x, y)\}$ and consider without loss of generality $\phi_m = 0$. We consider a finite number of scattering centers at each resolution cell (x, y) and reparametrize the scene reflectivity $g(x, y, z)$ as:

$$g_q(x, y) = g(x, y, h_q(x, y)) \tag{18}$$

where $g_q(x, y)$ denotes the reflectivity of the q'th scattering center at location $(x, y, h_q(x, y))$. In general the number of scatterers per resolution cell varies spatially and needs to be estimated from the data. Then, the ground plane image for elevation θ_i can can be written as:

$$I_p(x_l, y_l) = s(x, y) \star \sum_{q=1}^{Q(x_l,y_l)} g(x, y) e^{-j \tan(\theta_j) k_y^0 h_q(x,y)} e^{-jyk_y^0} \tag{19}$$

where $s(x,y)$ is the inverse Fourier transform of the 2-D windowing function used in imaging, $k_y^0 = (4\pi f/c)\cos(\bar{\theta})$ is the center frequency used in baseband modulation and $Q(x_l,y_l)$ is the number of scatterers in the resolution cell (x_l,y_l). The ground locations $(x,y,h_q(x,y))$ and the image coordinates (x_l,y_l) are related through layover :

$$x_l = x \qquad y_l = y + \tan(\theta_p)h_q(x,y). \tag{20}$$

We assume that the difference between the elevation angles for the different passes is small enough so that for each elevation pass the scattering center $(x,y,h_q(x,y))$, falls to the same resolution cell (x_l,y_l). Without loss of generality we consider $P+1$ circular passes at elevation angles $\theta_p = \bar{\theta} + p\Delta\theta$ for $p = -P/2,\ldots,P/2$. Then the baseband images from each pass can be modeled as:

$$I_p(x_l,y_l) = \sum_{q=1}^{Q(x_l,y_l)} \tilde{g_q}(x_l,y_l)e^{-jk_y^0\tan(\theta_p)h_q(x_l,y_l)} \tag{21}$$

using the approximation

$$\tan(\theta_p) \approx \tan(\bar{\theta}) + \frac{1}{\cos^2(\bar{\theta})}p\Delta\theta, \tag{22}$$

we obtain the sum of complex exponential model:

$$I_p(x_l,y_l) = \sum_{q=1}^{Q(x_l,y_l)} \tilde{g_q}(x_l,y_l)e^{-jk_q(x_l,y_l)p} \tag{23}$$

where the complex constant $e^{-j\tan(\bar{\theta})k_y^0 h_p(x_l,y_l)}$ is absorbed into the reflectivity $\tilde{g_q}(x_l,y_l)$ and the frequency factor k_q is given by:

$$k_q(x_l,y_l) = \frac{4\pi f}{c\cos(\bar{\theta})}\Delta(\theta)h_q(x_l,y_l) \tag{24}$$

The frequency estimates $\hat{k}_q$ are then transformed into height estimates $\hat{h}_q$ using:

$$\hat{h}_q = \hat{k}_q\frac{c\cos(\bar{\theta})}{4\pi f_c\Delta(\theta)}. \tag{25}$$

Each estimated scattering location $(x_l,y_l,h_p(x_l,y_l))$ is then mapped to image coordinates by inverting the equation (20) at the mean elevation angle $\bar{\theta}$:

$$x = x_l \qquad y = y_l - \tan(\bar{\theta})h_q(x_l,y_l). \tag{26}$$

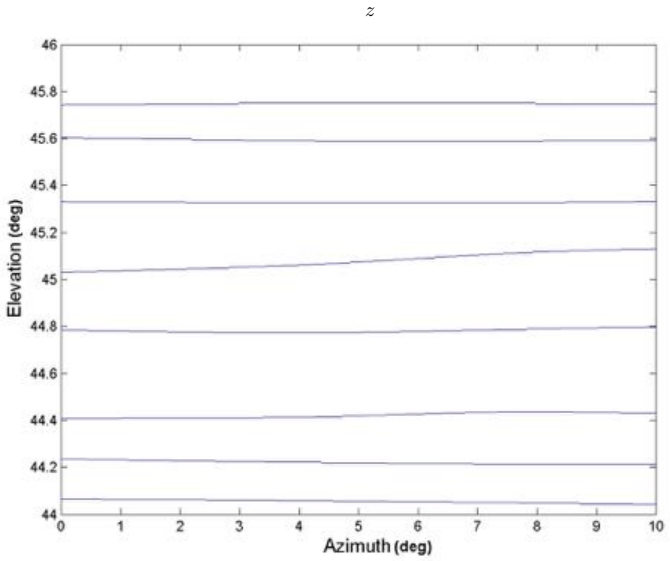

Figure 5: Variation in elevation angle over a 10° azimuth window. "Reproduced with permission from *IET Radar, Sonar and Navigation*, 4(3),2010. c IET 2010. "

Estimation of parameters of complex exponentials in noise is a fundamental problem in spectral estimation and array signal processing [27]. If the number of distinct complex exponentials is known, several high resolution methods can be used to estimate the frequencies. Model order selection for sum of complex exponential model have been studied widely in literature [28, 29].

In general, the elevation spacing of the CSAR flight paths are not equispaced. As an example, for the GOTCHA CSAR data collection experiment conducted by the Air Force Research Laboratory (AFRL) [12] features eight complete circular passes collected at nominal 45 degree elevation angle. Each pass has a planned (ideal) separation of $\Delta\theta = 0.18^\circ$ in elevation. Actual flight paths differ from the planned paths, with elevation samples at $44.27^\circ, 44.18^\circ, 44.1^\circ, 44.01^\circ, 43.92^\circ, 43.53^\circ, 43.01^\circ, 43.06^\circ$ degrees. In addition in each pass the elevation varied as the aircraft circled the scene. Figure 5 shows the variation in elevation angle over 10° azimuth window.

The harmonic retrieval problem of multiple complex exponential terms from a short, nonuniformly-sampled

data set is nontrivial; common techniques such as MUSIC do not readily apply since there is only one snapshot from which to form a covariance matrix estimate.

In the next subsections 1.5.1 and 1.5.2, we review two methods of spectral estimation that are applicable to CSAR collections with approximately parallel flight paths. The first technique is based on interpolation of the CSAR data to a uniformly spaced vertical grid using sparsity regularized least-square techniques and then use traditional spectral estimation methods such as ESPRIT [30] to the resulting oversampled covariance matrix. The second technique is based on the observation that majority of the pixels contain only a single scattering center in the height dimension. This single scatterer per resolution voxel approximation to the system model enables computationally efficient maximum-likelihood estimation using non-uniform discrete Fourier transform of the data.

1.5.1 Sparsity regularized interpolation approach to m-IFSAR

One approach to solve the spectral estimation problem from non-uniformly sampled data is to first interpolate to uniform grid and then apply classical technical techniques that rely on uniformly spaced samples. In particular, algorithms known as "interpolated array methods" estimate the output of a uniform virtual array by interpolating the outputs of the actual array [31,32]. The simplest method of interpolation is to use linear interpolation to a regular grid. As we will see in the simulation example, simple linear interpolation leads to degraded performance. Here, we outline a new interpolated array method based on sparsity regularized reconstruction of single pulse image $I_\phi(r,h)$ obtained by coherently processing returns for multiple elevations $\{\theta_p\}$ at a single azimuth angle ϕ. The range (r) and height (h) are measured with respect to slant plane coordinates.

The relationship between the single pulse image $I_\phi(r,h)$ and the projection of the scene reflectivity function

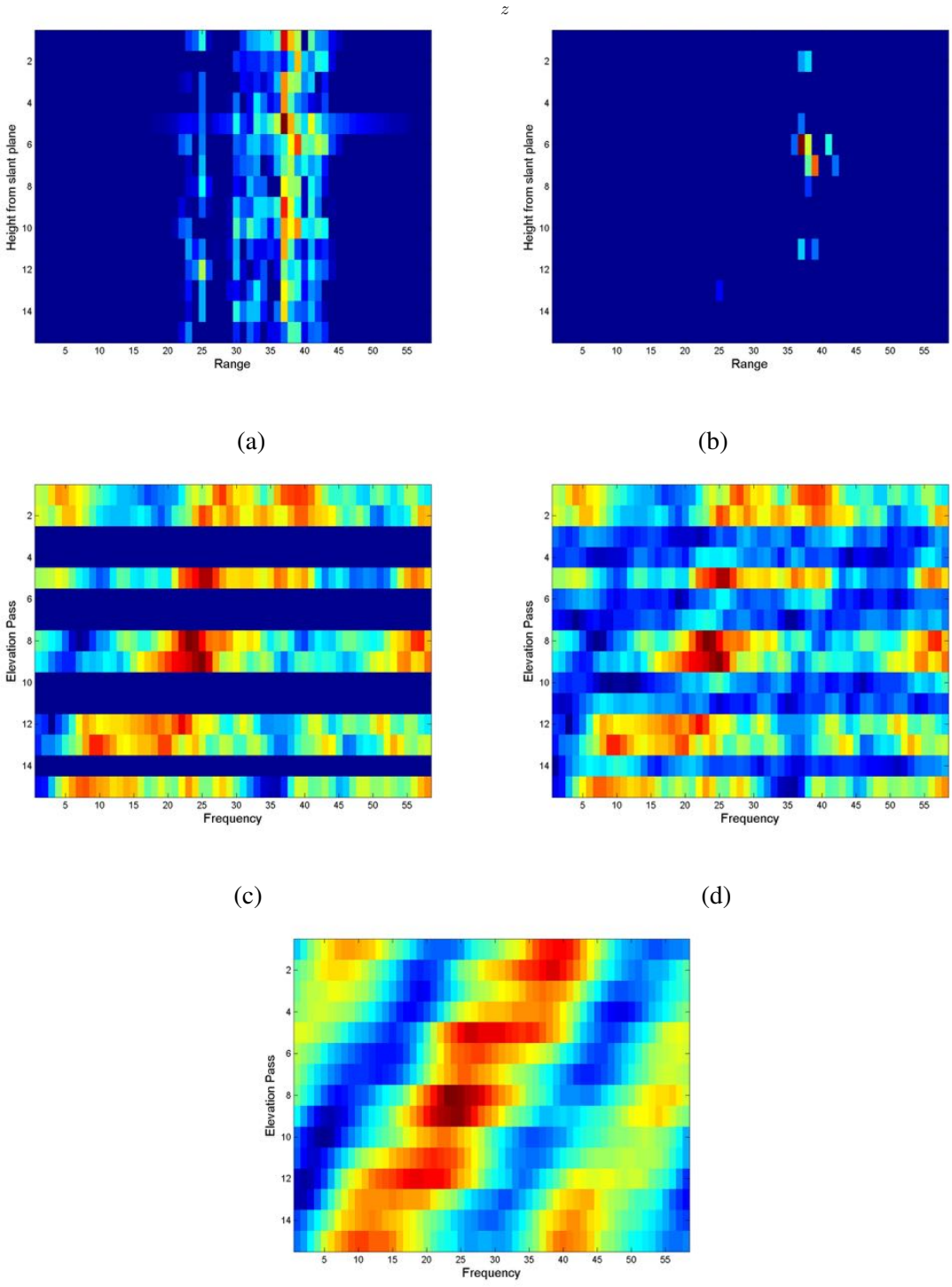

Figure 6: Single Pulse Image from eight nonuniform spaced elevation passes (a) original (b) sparsity regularized enhancement and the corresponding phase histories (c) original (d) linearly interpolated (e) sparsity regularized interpolation for λ = 0.1 and *p* = 1.0.

$g_\phi(r,h)$ on the azimuth plane ϕ is given by:

$$I_\phi(r,h) = \mathbf{\Phi}_\phi g_\phi(r,h) + n(r,h), \tag{27}$$

where $\mathbf{\Phi}_\phi$ is the convolution matrix of the system point spread function corresponding to the elevation spacing at azimuth angle ϕ and $n(r,h)$ represents noise and modeling errors. The deconvolution problem aims to reconstruct the scene reflectivity function $g_\phi(r,h)$ from the measured single puls image $I_\phi(r,h)$, given the knowledge of the convolution kernel $\mathbf{\Phi}_\phi$. The convolution kernel $\mathbf{\Phi}_\phi$ acts like a low-pass filter and does not have a bounded inverse, therefore in the absence of any constraints on $g_\phi(r,h)$, the deconvolution problem is ill-posed [33]. Here, we again consider the majorization-maximization method reviewed in section 1.4 , which enforces sparsity in the reconstruction process. Specifically, we obtain an enhanced single pulse image through minimization of :

$$\hat{g}_\phi(r,h) = \arg\min_g \left\{ \|I_\phi - \mathbf{\Phi}_\phi g\|_2^2 + \lambda \|g\|_p \right. \tag{28}$$

The first term in the minimization captures the consistency of the reconstructions with the observed data through equation (27); the second term in the minimization, favors sparse solutions for g for $p \leq 1$. The real valued scalar parameter λ controls the relative weight of the two factors and is determined based on the expected signal to clutter ratio [14]. The unconstrained optimization problem in (28) can be efficiently solved using an iterative pseudo-Newton method introduced in [16] and results in the location and amplitude of major scattering centers in the subaperture image. We note that a wide variety of methods have been proposed for the solution of (28) in the literature [34, 35].

Fourier inversion of the enhanced image $\hat{g}_\phi(r,h)$ results in phase histories from a virtual array with equal spacing. Once interpolated histories are found, the sum of complex exponential model given in (23) is applicable and therefore spectral estimation methods can be employed to detect and resolve scatterers in the height dimension at each pixel (x_l, y_l) in the slant-plane. Here, we employ a simple model order selection method based on thresholding the eigenvalues of the sample covariance matrix for the vector $\{I_p(x_l, y_l)\}_p$ to

estimate the model order $Q(x_l, y_l)$. Using this model order we then use the ESPRIT [30] method to estimate the frequencies $k_q(x_l, y_l)$ from the signal eigenvectors of the sample covariance matrix.

In the following, we illustrate sparsity regularized interpolated array method to multipass circular SAR data using the AFRL GOTCHA CSAR data set. Here we divided the data on 36 non-overlapping windows of width $\Delta = 10^\circ$ centered at $\phi_m \in \{0^\circ, 10^\circ, \ldots, 350^\circ\}$ and used the entire 640 MHz bandwidth centered at 9.6 GHz for the single VV polarization. For each subaperture window, we created a virtual array of 32 uniformly sampled passes covering the same elevation range achieved by the SAR sensor in that subaperture. Using the sparsity regularized interpolation method, we interpolated the phase history data collected at nonlinear flight paths to the data collected at virtual array geometry. In constructing the single pulse images we used the prior knowledge about the target dimensions to restrict the height and range support of the single pulse image to 5 meters. For each of the virtual 32 passes and for each of the subapertures ground plane images are constructed using classic backprojection. Next, we applied ESPRIT based parametric spectral estimation method to all pixels whose amplitude is within the 20dB of image maximum, to construct three dimensional points representing observed strong scattering mechanisms. The 3-D point clouds from each subaperture window is rotated and overlayed to a common reference frame.

Figure 7 shows the resulting reconstruction overlayed with the CAD model of the station wagon. We observe that point cloud encompasses the CAD model and strong returns from the ground plane-side panel (double bounce mechanism) and the curved surfaces (single bounce mechanism) are clearly visible. We note that the car was parked on smooth asphalt surface with no close by cars or buildings that would have introduced multipath reflections.

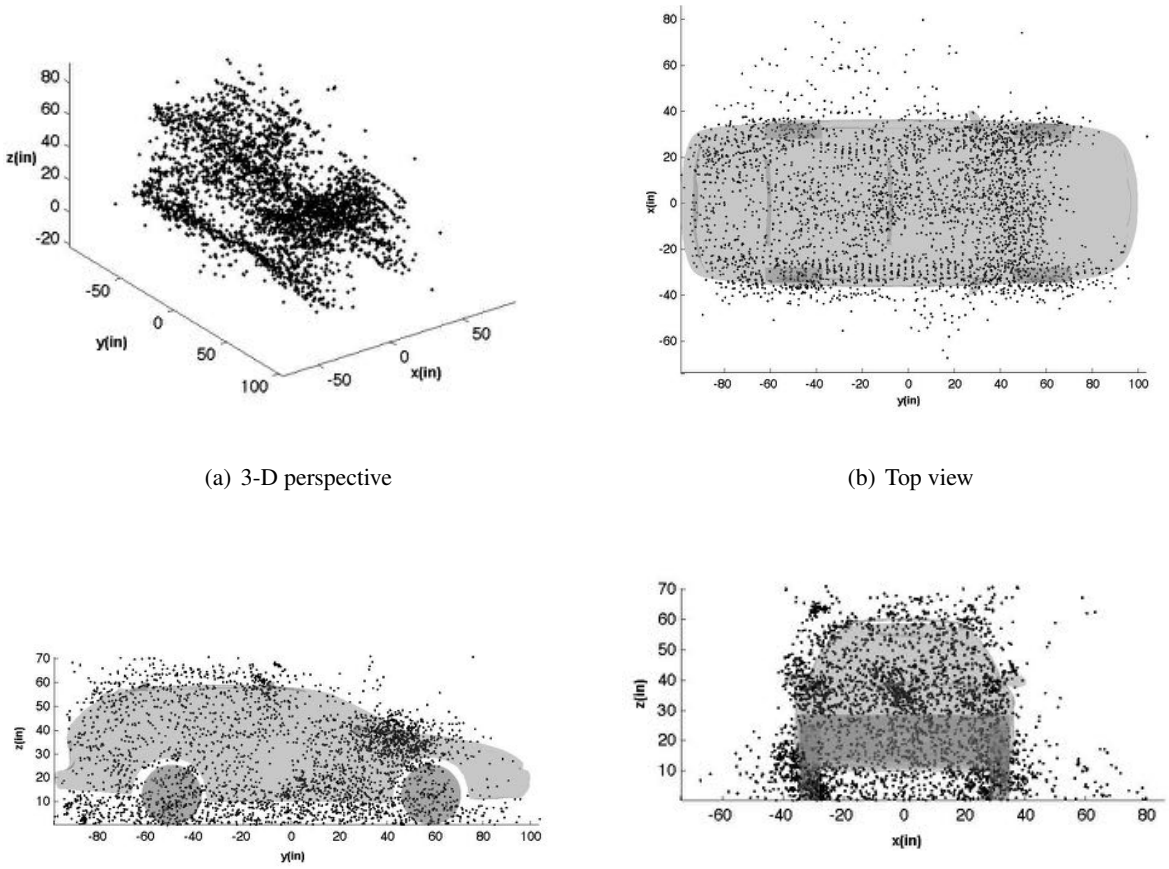

(a) 3-D perspective

(b) Top view

(c) Side view

(d) Front view

Figure 7: Three dimensional reconstruction of a Taurus Station Wagon using multipass Circular SAR data.

1.5.2 DFT peak detection approach for m-IFSAR

For many vehicles the horizontal imaging geometry ensures that only few scatterers are present in each image pixel (x_l, y_l). Specifically, in a recent study using CSAR simulated X-band data of vehicles [3], the estimated model order was $Q = 1$ in a large majority of cases. Thus, the complex exponential signal model considered in (23) is sparse, with typically only 1 scattering center in the height dimension. This presents a computational advantage, because for the single-exponential case, a maximum likelihood estimator of its frequency in white measurement noise is given by the peak of the Fourier transform of the data, and this Fourier transform is easy to compute even in the case of non-uniform samples. We can thus estimate, for

each pixel (x_l, y_l) the location $k_p(x_l, y_l)$, as the peak of the Fourier transform of the non uniformly sampled values for that pixel and calculate the height using (26). The complex amplitude of the Fourier transform at the peak provides an estimate of the amplitude of the scattering center.

We note that using this multi-pass IFSAR approach, the original 3-D problem has been converted to a set of 2-D and 1-D processing steps. First, 2-D images are formed for each azimuth subaperture and each elevation angle. Then, 1-D processing is applied to each $P \times 1$ vector obtained by stacking the set of P elevation images and selecting the P values at a pixel location of interest. The processing reduction is afforded by the particular structure of the sparse measurement geometry provided by CSAR collections.

In general for the multi-pass IFSAR approach, reconstructed scattering centers are not constrained to lay on a grid in the height dimension. To have a volumetric image defined on a uniform grid, data should be first interpolated to a grid with uniform voxel spacing in each dimension. Empirically we have found that a Gaussian kernel with standard deviation of grid-spacing provides visually appealing results when used for interpolation.

Figure 8 shows the results of the multi-pass IFSAR approach applied to the CSAR GOTCHA data for Toyota Camry, previously used to illustrate the performance of direct sparsity regularized approach shown in Figure 4. The top 20 dB points are shown. The results are shown for VV polarization. Scattering is assumed to be above the ground plane in calculations; so, unlike in the L_p regularized LS reconstruction, there are no non-zero voxels below the vehicle. As in the L_p regularized LS reconstruction, a set of 72 subaperture image sets were formed, each with 5° azimuth extent, and the image-domain subaperture reconstructions were combined using (8).

The multi-pass IFSAR reconstructions appear to be more filled than the L_p regularized LS reconstructions. This is due to relatively lower downrange and crossrange resolution of the Fourier imaging techniques employed. The detriment of spatial spread is application specific. For visualization, this spreading may

Figure 8: Wide angle multi-pass IFSAR reconstructions of a civilian vehicle from GOTCHA dataset (3-D, Side and Top Views).

be desirable, favoring the multi-pass IFSAR reconstructions. In other applications, such as ATR, fine 3-D resolution features may be desirable, and L_p regularized LS reconstructions may be superior.

1.6 Practical Considerations: Autofocus and Registration

In this chapter, we have reviewed several methods for 3-D target reconstruction using sparsity assumption on the target support. All these methods can provide high-resolution volumetric imagery from multipass circular SAR collections, provided that data from the multiple passes are properly registered and phase coherent. While many system errors have decreased with improved collection platform reference systems and more accurate clocks, remaining system errors still degrade imagery. Many system errors, such as platform position errors, manifest as phase errors, be it pulse to pulse or pass to pass. An oscillator scale factor error may induce different spatial translations of 2-D imagery. Amplifier thermal effects or aspect dependent antenna gain may adversely effect gain across passes. The strong requirement for phase coherence in SAR dictates these errors be very small. For instance, Jakowatz [36] suggests no more than $\frac{\pi}{4}$ radians of phase error, equivalently small relative range error, be tolerated for acceptable autofocus of pulse-to-pulse errors. Autofocus aims to estimate these errors from the radar data and compensate them. While

several effective methods exist for within pass collections, such as Phase Gradient Autofocus [36], other methods are needed for 3-D autofocus in situations when wide-aspect persistent scatterers are not available for prominent point autofocus [37]. Recently, interpass 3-D autofocus methods have been proposed [38–40]. These autofocus methods can be formulated as a set of linear filters in the spatial frequency domain for each p'th pass,

$$H_p(k_x, k_y) = e^{c_p + j\theta_l + j2\pi(x_p k_x + y_p k_y)}, \tag{29}$$

where c_p is a constant gain term, θ_l is a constant phase term, and (x_l, y_l) is a linear phase term in the frequency domain or equivalently a (x_l, y_l) translation in the image domain in accordance with the Fourier shift theorem. The image domain filter is expressed as $h_l(x, y) = \mathcal{F}^{-1}\{H_l(k_x, k_y)\}$. The application of the registration filters can be performed in spatial domain as:

$$\bar{I}_p(x, y; \Theta) = I_p(x, y) * h_j(x, y, \Theta) \tag{30}$$

The autofocus problem may be posed as a joint optimization problem. Considering P elevation passes, the registration filter of equation (29) specifies a parameter vector of

$$\Theta = \begin{bmatrix} c_1 & \dots & c_{P-1} & \theta_1 & \dots & \theta_{P-1} & (x,y)_1 & \dots & (x,y)_{P-1} \end{bmatrix}^T, \tag{31}$$

where the registration parameters for one of the P passes is held constant or fixed to some ground calibration feature to avoid ambiguity. The autofocus problem is to find Θ^* that jointly minimizes some appropriate objective function $C(\{\bar{I}_p(x, y, \Theta)\})$ that evaluates coherency of the multi pass data:

$$\Theta^* = \arg\min_{\Theta} C(\{\bar{I}_p(x, y, \Theta)\}). \tag{32}$$

Interpass 3-D autofocus methods in the literature [38–40] differ in their optimization criteria. Kragh [39] considers Rényi entropy over the normalized voxel energy of the volumetric images as the optimization metric for 3-D autofocus.

$$S_\alpha(\boldsymbol{g}) = \frac{1}{1-\alpha} \log \sum_{n=1}^{N} q_n^\alpha, \tag{33}$$

where $\alpha > 0$ is the entropy order parameter. To compute entropy over a volumetric image, let $\boldsymbol{g} = (g_1, \ldots, g_N)$ be a vector of image samples from $\bar{I}(x, y, z; \Theta)$ obtained from focused ground plane imagery using (2), and let $q_n = |g_n|^2 / \sum_n |g_n|^2$ be the normalized voxel energy. Evaluating the Rényi entropy for $\alpha = 2$ gives the quadratic entropy criterion of the image used for autofocus:

$$C(\bar{I}_p(x, y; \Theta)) = 2 \log \sum_{n=1}^{N} |g_n|^4 + 2 \log \sum_{n=1}^{N} |g_n|^2 \quad . \tag{34}$$

Elkin [38] considers the least-squares (LS) optimization criteria as sum over the image, using the model order assumption of one for the height dimension to obtain a single scatterer at height $z^*(x, y)$ per image pixel (x, y).

$$C(\{\bar{I}_p(x, y; \Theta)\}) = \sum_{x,y} \sum_{p} |I_p * h_p(x, y, \Theta)|^2 - \frac{1}{P} \left| \sum_{p} (I_p * h_p(\Theta))_{(x,y)} e^{-jk_y^0 \tan(\theta_p) z^*(x,y)} \right|^2 . \tag{35}$$

Boss [40] proposed a 3-D autofocus method based on maximizing coherence factor computed over the dominant scatterers in an image scene given by:

$$C(\{\bar{I}_p(x, y; \Theta)\} = \sum_{x,y} \frac{\left| \sum_p (I_p * h_p(\Theta))_{(x,y)} e^{-jk_y^0 \tan(\theta_p) z^*(x,y)} \right|^2}{P \sum_p |I_p * h_p(x, y, \Theta)|^2} \tag{36}$$

We note that for a typical registration problem the total energy of the registered images is constant therefore the least square criterion simplifies to:

$$\Theta^* = \arg\max_{\Theta} \sum_{x,y} \left| \sum_{p} (I_p * h_p(\Theta))_{(x,y)} e^{-jk_y^0 \tan(\theta_p) z^*(x,y)} \right|^2 \quad . \tag{37}$$

which is equivalent to maximizing the DFT amplitudes of the registered images (or equivalently summing up the numerator of the Coherence Factor). As a result LS registration emphasizes coherence of higher amplitude pixels which could be preferable in certain applications, whereas Coherence Factor metric provides the flexibility to target a set of pixels (for example pixels on target), maximizing coherence across those pixels with equal weight.

2.0 References

[1] E. Ertin, L.C. Potter, and R.L. Moses, "Enhanced imaging over complete circular apertures," in *Fortieth Asilomar Conf. on Signals, Systems and Computers (ACSSC 06)*, Oct 29 – Nov. 1 2006, pp. 1580–1584.

[2] E. Ertin, C. D. Austin, S. Sharma, R. L. Moses, and L. C. Potter, "GOTCHA experience report: Three-dimensional SAR imaging with complete circular apertures," in *Algorithms for Synthetic Aperture Radar Imagery XIV*, E. G. Zelnio and F. D. Garber, Eds., Orlando, FL., April 9–13 2007, SPIE Defense and Security Symposium.

[3] E. Ertin, R. L. Moses, and L. C. Potter, "Interferometric methods for 3-D target reconstruction with multi-pass circular SAR," *IET Radar, Sonar and Navigation*, vol. 4, no. 3, 2010.

[4] C. D. Austin and R. L. Moses, "Wide-angle sparse 3D synthetic aperture radar imaging for nonlinear flight paths," in *IEEE National Aerospace and Electronics Conference (NAECON) 2008*, July 16–18 2008, pp. 330–336.

[5] C. D. Austin, E. Ertin, and R. L. Moses, "Sparse multipass 3D SAR imaging: Applications to the GOTCHA data set," in *Algorithms for Synthetic Aperture Radar Imagery XVI*, E. G. Zelnio and F. D. Garber, Eds., Orlando, FL., April 13–17 2009, SPIE Defense and Security Symposium.

[6] N. Ramakrishnan, E. Ertin, and R. Moses, "Enhancement of coupled multichannel images using sparsity constraints," *IEEE Transactions on Image Processing*, Aug 2010.

[7] C. D. Austin, E. Ertin, and R. L. Moses, "Sparse signal methods for 3-D radar imaging," *IEEE Journal of Selected topics in Signal Processing*, vol. 5, no. 3, 2011.

[8] K.E. Dungan and L. C. Potter, "3-D imaging of vehicles using wide aperture radar," *IEEE Trans. on AES*, vol. 47, no. 1, 2011.

[9] A. Budillon, A. Evangelista, and G. Schirinzi, "Three-dimensional sar focusing from multipass signals using compressive sampling," *IEEE Trans. Geosci. Remote Sens.*, vol. 49, no. 1, pp. 488–499, 2011.

[10] X. Zhu and R. Bamler, "Super-resolution power and robustness of compressive sensing for spectral estimation with application to spaceborne tomographic sar," *IEEE Trans. Geosci. Remote Sens.*, vol. 50, no. 1, pp. 247–258, Jan 2012.

[11] X. Zhu and R. Bamler, "Demonstration of super-resolution for tomographic sar imaging in urban environment," *IEEE Trans. Geosci. Remote Sens.*, vol. 50, no. 8, pp. 3150–3157, Aug 2012.

[12] C. H. Casteel, L. A. Gorham, M. J. Minardi, S. Scarborough, and K. D. Naidu, "A challenge problem for 2D/3D imaging of targets from a volumetic data set in an urban environment," in *Proc. SPIE 6568*, E. G. Zelnio and F. D. Garber, Eds., Apr 2007.

[13] C. V. Jakowatz and P. A. Thompson, "A new look at spotlight mode synthetic aperture radar as tomography: imaging 3D targets," *IEEE Trans. Image Processing*, vol. 4, no. 5, May 1995.

[14] R. Moses, L. Potter, and M. Çetin, "Wide angle SAR imaging," in *Algorithms for Synthetic Aperture Radar Imagery XI (Proc. SPIE Vol. 5427)*, Edmund G. Zelnio, Ed., Apr. 2004.

[15] R. L. Moses and L. C. Potter, "Noncoherent 2D and 3D SAR reconstruction from wide-angle measurements," in *13th Annual Adaptive Sensor Array Processing Workshop*, Lexington, MA, June 2005, MIT Lincoln Laboratory.

[16] M. Cetin and W. C. Karl, "Feature enhanced synthetic aperture radar image formation based on nonquadratic regularization," *IEEE Trans. Image Processing*, vol. 10, pp. 623–631, Apr 2001.

[17] T. Kragh and A. Kharbouch, "Monotonic iterative algorithms for sar image restoration," in *IEEE 2006 Int. Conf. on Image Processing*, Oct 2006, pp. 645–648.

[18] M. Figueiredo, R. Nowak, and S. Wright, "Gradient projection for sparse reconstruction: Application to compressed sensing and other inverse problems," *IEEE Journal of Selected Topics in Signal Processing*, vol. 1, no. 4, pp. 586–597, Dec 2007.

[19] A. Beck and M. Teboulle, "A fast iterative shrinkage-thresholding algorithm for linear inverse problems," *SIAM Journal of Imaging Sciences*, vol. 2, no. 1, pp. 183–202, 2009.

[20] I. Daubechies, M. Defrise, and C. D. Mol, "An iterative thresholding algorithm for linear inverse problems with a sparsity constraint," *Comm. Pure Appl. Math*, vol. 57, no. 11, pp. 1413–1467, 2004.

[21] T. Goldstein and S. Osher, "The split Bregman method for L1-regularized problems," *SIAM Journal on Imaging Sciences,*, vol. 2, no. 2, pp. 323–343, 2009.

[22] R. Saab, R. Chartrand, and O. Yilmaz, "Stable sparse approximations via nonconvex optimization," *33rd International Conference on Acoustics, Speech, and Signal Processing (ICASSP)*, 2008.

[23] L. Greengard and J. Y. Lee, "Accelerating the nonuniform fast fourier transform," *SIAM Review*, vol. 43, no. 3, pp. 443–454, 2004.

[24] J. Fessler and B. Sutton, "Nonuniform fast fourier transforms using min-max interpolation," *IEEE Transactions on Signal Processing*, vol. 51, no. 2, pp. 560–574, Feb 2003.

[25] S. Xiao and D. C. Munson, "Spotlight-mode SAR imaging of a three-dimensional scene using spectral estimation techniques," in *Proceedings of IGARSS 98*, 1998, vol. 2, pp. 624–644.

[26] F. Gini and F. Lombardini, "Multibaseline cross-track SAR interferometry: a signal processing perspective," *IEEE AES Magazine*, vol. 20, no. 8, pp. 71–93, Aug 2005.

[27] P. Stoica and R. Moses, *Spectral Estimation of Signals*, Prentice Hall, 2005.

[28] M. Wax and T. Kailath, "Detection of signals by information theoretic criteria," *IEEE Trans. ASSP*, vol. 33, pp. 387–392, April 1985.

[29] D. N. Lawley, "Tests of significance of the latent roots of the covariance and correlation matrices," *Biometrica*, vol. 43, pp. 128–136, 1956.

[30] R. Roy and T. Kailath, "ESPRIT-estimation of signal parameters via rotational invariance tecniques," *IEEE Trans. ASSP*, vol. 37, no. 7, pp. 984–995, 1989.

[31] B. Friedlander, "The root-MUSIC algorithm for direction finding in interpolated arrays," *Signal Processing*, vol. 30, no. 1, pp. 15–19, Jan 1993.

[32] F. Bordoni, F. Lombardini, F. Gini, and A. Jacabson, "Multibaseline cross-track sar interferometry using interpolated arrays," *IEEE Trans. on AES*, vol. 41, no. 4, pp. 1472–1481, Oct 2005.

[33] H. Stark, Ed., *Image Recovery: Theory and Application.*, Academic Press, Orlando, FL, 1987.

[34] S Wright, R Nowak, and M Figueiredo, "Sparse reconstruction by separable approximation," *IEEE International Conference on Acoustics, Speech and Signal Processing, (ICASSP 2008)*, pp. 3373 – 3376, Mar 2008.

[35] K Herrity, R Raich, and A Hero, "Blind deconvolution for sparse molecular imaging," *IEEE International Conference on Acoustics, Speech and Signal Processing, (ICASSP 2008)*, pp. 545 – 548, Mar 2008.

[36] C. V. Jakowatz Jr., D. E. Wahl, P. H. Eichel, D. C. Ghiglia, and P. A. Thompson, *Spotlight-Mode Synthetic Aperture Radar: A Signal Processing Approach*, Kluwer Academic Publishers, Boston, 1996.

[37] M. Ferrara, J. A. Jackson, and C. Austin, "Enhancement of multi-pass 3D circular SAR images using sparse reconstruction techniques," in *Algorithms for Synthetic Aperture Radar Imagery XVI*, E. G. Zelnio and F. D. Garber, Eds., Orlando, FL., April 13–17 2009, SPIE Defense and Security Symposium.

[38] F. L. Elkin, "Autofocus for 3D imaging," in *Proceedings of SPIE 6970*, E. G. Zelnio and F. D. Garber, Eds., Apr 2008.

[39] T. J. Kragh, "Minimum-entropy autofocus for three-dimensional SAR imaging," in *Proc. SPIE 7337*, E. G. Zelnio and F. D. Garber, Eds., Apr 2009.

[40] N. Boss, E. Ertin, and R. Moses, "Autofocus for 3d imaging with multipass sarfeature extraction algorithm for 3D scene modeling and visualization using monostatic SAR," in *Algorithms for Synthetic Aperture Radar Imagery XVII*, Edmund G. Zelnio and Frederick D. Garber, Eds., Apr 2010, vol. 7699 of *Proceedings of SPIE*.